JOURNAL OF AIRCRAFT
Vol. 46, No. 4, July–August 2009

Transport Wing Flutter Model Transonic Limit Cycle Oscillation Test

John W. Edwards,* Charles V. Spain,† Donald F. Keller,‡ and Robert W. Moses§
NASA Langley Research Center, Hampton, Virginia 23681-2199
and
David M. Schuster¶
NASA Engineering and Safety Center, Hampton, Virginia 23681-2199

DOI: 10.2514/1.30079

The model for aeroelastic validation research involving computation semispan wind-tunnel model, a transport wing–fuselage flutter model, was tested in NASA Langley's Transonic Dynamics Tunnel with the goal of obtaining experimental limit cycle oscillation behavior data at transonic separation onset conditions. This research model is notable for its inexpensive construction and instrumentation installation procedures. Unsteady pressures and wing responses were obtained for three wing-tip configurations: clean, tip store, and winglet. Traditional flutter boundaries were measured over the range of $M = 0.6$–0.9, and maps of limit cycle oscillation behavior were made in the range of $M = 0.85$–0.95. The effects of dynamic pressure and angle of attack were measured. Testing in both R134a heavy gas and air provided unique data on the Reynolds number, transition effects, and the effect of speed of sound on limit cycle oscillation behavior. This report gives an overview of the test results, including experimental flutter boundaries, and the conditions involving shock-induced transonic flow separation onset at low wing angles, including maps of limit cycle oscillation behavior.

Introduction

THE models for aeroelastic validation research involving computation (MAVRIC) project was undertaken by NASA Langley Research Center's Aeroelasticity Branch with the goal of obtaining experimental wind-tunnel data at transonic separation onset conditions. The aeroelastic response behavior referred to as limit cycle oscillation (LCO) was the primary target. LCO behavior is characterized by rather constant amplitude, periodic structural response at selective frequencies, which are usually recognizable as being those of the aeroelastically loaded structure. Bunton and Denegri [1] discussed LCO characteristics of fighter aircraft, and Denegri [2] provided test cases from flight tests of the F-16 aircraft for three classes of response, classical flutter, typical LCO, and nontypical LCO, which are very well suited for use as computational test cases. Cunningham [3,4], Meijer and Cunningham [5], and Meijer [6] also described LCO experience on the F-16 aircraft and presented results of semi-empirical modeling of the LCO phenomenon. Although their formulation is general, the focus of the applications has been upon LCOs encountered between angles of attack of 5–10 deg and involving interaction of leading-edge vortex flows, tip flows, and normal wing shocks. In contrast, the test cases of [2] are all for 1 *g* level flight at transonic speeds, at which there are no leading-edge vortex flows. This brings into focus a key feature of LCO behavior: incidents of (aerodynamically induced) LCO are found for flowfields featuring transitions or boundaries between differing flow states. A prime example is the onset of separated flow over some portion of an aircraft's lifting surfaces. Furthermore, the LCO is typically limited to a narrow region in Mach number and/or angle of attack signaling the change in flow state, such as separation onset. LCO occurrences are common on fighter aircraft; Norton [7] describes incidents on F-5, F-16, F-111, F-15 short takeoff and landing, and F/A-18 aircraft. LCOs induced by structural nonlinearities have been widely reported in the literature and are not considered in this paper.

Incidents of LCO are not limited to fighter aircraft. LCOs are reported by Jacobson et al. [8] and Dreim et al. [9] involving wing-bending interaction with rigid-body pitching and plunging on the B-2 bomber, and Edwards [10] reported LCO behavior on a transport wing wind-tunnel flutter model. Because LCO behavior is closely related to subcritical flutter behavior (e.g., aeroelastic response at speeds near but below the flutter speed, with the attendant very low damping levels), attempts to study the behavior with wind-tunnel flutter models have been made. The attempts are frequently unsuccessful due to lack of knowledge of the necessary ingredients producing LCO, the inability to fully simulate full-scale aircraft conditions in wind-tunnel testing (model angle of attack and the mean deformed wing shape are not matched in common scaling and testing procedures), and the differing dynamic testing conditions between flight and wind tunnel. The wind-tunnel testing environment has much more moderate frequency turbulence than atmospheric flight conditions, resulting in continuously disturbed model motions that mask the subtleties of LCO behavior. Several wind-tunnel tests have reported unintentional LCO behavior observed during aeroelastic/flutter testing: Gránásy et al. [11] found two branches of LCO behavior extending well below the flutter boundary for a high aspect ratio, elastic, actively controlled wing model; NASA's ARW-2 (supercritical, high aspect ratio, aeroelastic research wing) [12,13] exhibited a region of high dynamic response in its first wing-bending mode; and NASA's high speed civil transport flexible semispan model [14] exhibited two regions of LCO-like response, one a broader region of "high dynamic response" in the first bending mode and the other a narrow chimney of high response. At the highest tested pressure, flutter and model failure were encountered in this chimney region. The latter two cases, along with numerous other unsteady pressure experiments in the NASA Langley Transonic Dynamics Tunnel, are summarized in [15]. One final, recent wind-tunnel test is that of a two-dimensional pitching and plunging

Presented as Paper 1291 at the AIAA/ASME/ASCE/AHS/ASC Structures, Structural Dynamics, and Materials Conference, Seattle, WA, 16–19 April 2001; received 28 January 2007; revision received 16 December 2008; accepted for publication 16 December 2008.

*Senior Research Engineer, Aeroelasticity Branch, Retired. Fellow AIAA.
†Senior Research Engineer, Aeroelasticity Branch, Retired.
‡Aerospace Engineer, Aeroelasticity Branch.
§Senior Research Engineer, Atmospheric Flight and Entry Systems Branch. Member AIAA.
¶NASA Technical Fellow for Aerosciences. Associate Fellow AIAA.

supercritical airfoil model [16]. LCO behavior was measured that agreed with flutter motions calculated with a Navier–Stokes code and a frequency domain modal superposition flutter solution.

It is interesting to note a connection between the current focus on LCO phenomena and long-standing aeroelastic response behaviors such as buffeting and buffet onset, control surface buzz, and angle-of-attack effects. One of the first experimental studies of nonlinear transonic effects on flutter was Erickson's [17] flutter and buffet tests of an early version of a space shuttle wing. Angle-of-attack and transition effects on damping were found over a very narrow transonic Mach range, and "limited amplitude flutter motions" and destructive wing flutter were encountered. Farmer et al. [18] studied the effect of supercritical and conventional wing profiles upon transonic flutter. Unpublished results of the effect of angle of attack upon flutter are similar in nature to those already described. Moss and Pierce [19] documented a case of torsional wing "buzz" at buffet onset conditions on a solid steel model. For the 27 deg leading-edge wing sweep, the main wing shock and the separated flow behind it aligned with the torsion mode node line, providing the driving mechanism for the buzz LCO.

Because of the difficulty of capturing LCO behavior in wind-tunnel tests, its occurrence in the tests of the aforementioned transport wing flutter model [10] led to its selection for further testing as the MAVRIC transport wing flutter model. Because of its simple aluminum plate construction, the model has the strength to withstand large dynamic wing motions without failing, making it ideal for the study of LCO behavior. This paper presents an overview of the wind-tunnel test, including details of the model construction, refurbishment, and instrumentation, followed by a description of the data system used for measuring the wing response and unsteady wing pressures. Testing of the model with three different wing-tip configurations, in both air and R134a heavy gas, is discussed. Finally, test results are summarized in the form of calculated (linear aerodynamics) and experimental flutter boundaries and maps of regions of LCO response behavior.

Model Construction, Refurbishment, and Instrumentation

The unmodified transport wing flutter model was tested previously in NASA Langley's Transonic Dynamics Tunnel (TDT) in 1993 and 1994. It is a semispan model of a transport wing design constructed of a stepped thickness aluminum plate planform and covered with end-grain balsa wood to provide the wing contour. The wing has no twist or dihedral, reflecting its original purpose of providing wind-tunnel flutter test data for calibration of analysis methods, and it was tested on the tunnel sidewall, low-mounted on a fuselage body of revolution. The plate structural construction method results in flutter models with sufficient strength to withstand oscillation amplitudes much larger than more typical flutter model construction methods can withstand without sustaining damage. Inspection of the previous test results indicated that the model exhibited LCO behavior at the higher transonic Mach numbers tested. Thus, the model was selected for retesting as the MAVRIC transport wing flutter model.

Figure 1 shows the refurbished model mounted on the TDT sidewall. The refurbishments included a new streamlined aft fuselage section, a new streamlined underwing belly-pan fairing, a new wing-tip body of revolution for the clean wing configuration, and extensive new instrumentation. The fuselage consisted of bodies of revolution integrated with a new 4 in. standoff section to account for the wall boundary layer. The original aft fuselage closure was a straight-sided conical section commencing at the wing trailing edge, which aggravated wing–fuselage juncture flow separation. The new aft fuselage was extended 6 in. and contained a 24 in. circular arc section closure with a sharp trailing edge. The new belly-pan closure was designed to minimize forward- and aft-facing curvatures and to meld smoothly with the wing lower surface.

Figure 2a shows the wing planform and instrumentation layout (described next), whereas Fig. 2b shows the stepped aluminum plate and end-grain balsa wood upper and lower surfaces. The plate thickness steps from 0.276 to 0.106 in. in four steps over the

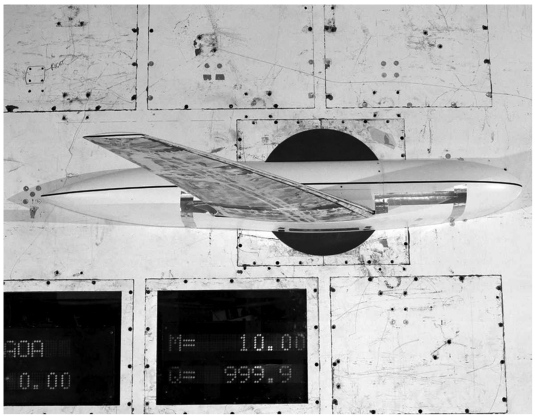

Fig. 1 MAVRIC model mounted on tunnel sidewall.

wingspan. The wing has a taper ratio of 0.29, a midchord sweep angle of 23 deg, and a span, S, of 53.17 in. The wing thickness varies from 13 (extrapolated to the symmetry plane) to 8.5% at the wing tip (based on the local chord length).

Figure 3 shows the three wing-tip configurations tested: clean wing tip (body of revolution), pencil tip store, and winglet. They are attached to the wing tip with three mounting screws. The winglet, also used in the 1994 test, is canted 75 deg from the wing plane and has a 41 deg leading-edge sweep. The pencil tip store was constructed to match the properties of the original winglet used in the 1993 test and, thus, has different mass properties than the present winglet.

The model is instrumented with 84 differential unsteady pressure sensors at three spanwise chords, 8 miniature piezoelectric accelerometers, and root bending and torsion strain gages. A servo-accelerometer measuring the model angle of attack was also mounted to the wing plate root. Bending and torsion strain gauges were also bonded to the wing plate root inside of the fuselage housing, where the bolt restraints at the root caused the torsion strain gauge to be ineffective.

Figure 4 shows the wing lower surface and fuselage. Also, routing troughs for the instrumentation are visible on the lower wing surface. The upper surface (not shown) has similar instrumentation routings. The 4 in. standoff of the fuselage from the wind-tunnel wall is clearly visible. Spanwise measurements are referenced to buttock line 0.00 in., which is located at the centerline of the fuselage body of revolution, abutting the standoff.

Eight accelerometers were mounted to the bottom of the wing plate at locations as near as allowed by the wing contour thickness to the leading and trailing edges at span stations $y = 14$, 24, 36, and 48 in. ($y/S = 0.26$, 0.45, 0.68, and 0.90). The wing contour at these locations was restored by filling the cavities with a silicone sealant. This filling resulted in detrimental straining of the accelerometer casings under strained conditions, and in situ calibrations of the accelerometers were required Also, optical targets were installed on the wing lower surface for use by the videogrammatic model deformation system [20]. This system was capable of recording dynamic model deformations at a rate of 60 frames per second. Late in the test, the wing upper surface was tufted to visually observe the extent of flow separation and make correlations with regions of LCO activity.

An attractive detail of the MAVRIC model's construction and instrumentation procedures is their low cost relative to standard procedures. Although the structural metal plate and end-grain balsa wood fabrication method is not favored for models requiring similitude with full-scale aircraft, it is quite adequate in producing models devoted to computational method validation and is much less expensive. A similar economy was followed in selecting the method for instrumenting the model. With the end-grain balsa wood in place and no desire to modify the wing profile (the LCO behavior of the model was to be preserved), the decision was made to install instrumentation using minimally invasive surface routing of the balsa

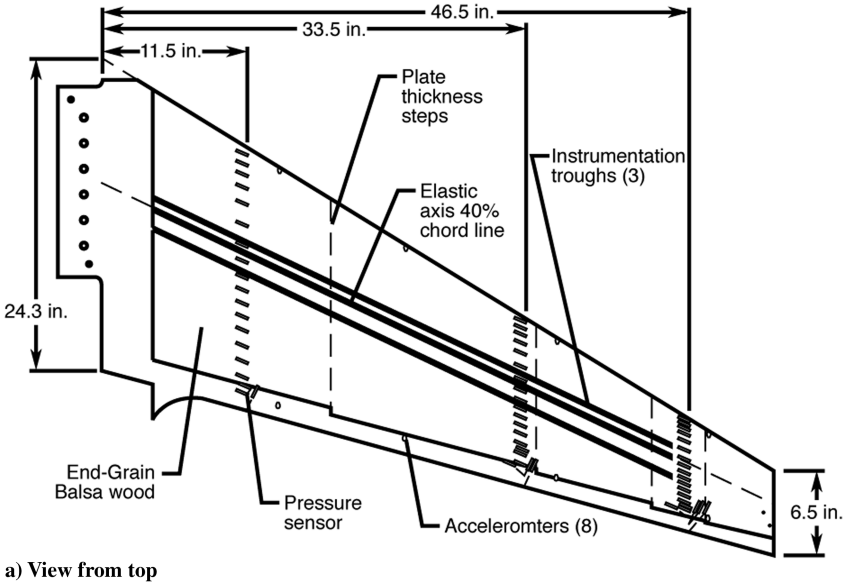

a) View from top

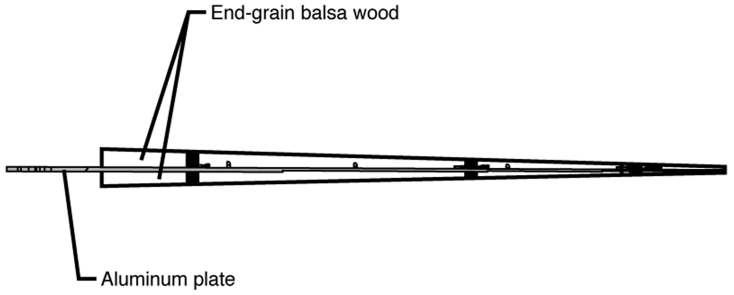

b) View from rear

Fig. 2 Layout of wing and instrumentation.

wood. Figure 5 shows the routing troughs for the mid- and outboard upper surface chords of the pressure sensors during fabrication.

Figure 6 indicates the method for assembling the pressure sensor mounting blocks, which included the 0.020 in. surface orifices. Shown from the bottom to the top are a pressure sensor, a protective metal sleeve, a mounting block with orifice hole, and the assembled mounting. The 0.5-in.-long 2.0 psi differential sensors were sealed inside the protective sleeves, which were then sealed into the mounting blocks already installed in the wing and covered with a filler material. The routed troughs containing reference pressure tubing and electrical wiring were covered with balsa strips and smoothed to the wing contour. The sensor reference tubes were connected to pressure manifolds located in the routed troughs. The manifolds were connected to the wind-tunnel plenum chamber by tubing. The three chords of pressure sensors were located at span stations $y = 11.5, 33.5,$ and 46.5 in. ($y/S = 0.22, 0.63,$ and 0.87). At each station, 18 upper surface and 10 lower surface pressure orifices were located as indicated in Table 1. In the following sections, upper (U) and lower (L) surface pressures and pressure coefficients are labeled for the inboard (I), middle (M), and outboard (O) sensor locations (e.g., PMU_{44} and $CPMU_{44}$ for the upper, middle sensor measurement at $x/C = 0.44$).

Following completion of the installation of the instrumentation, the wing surface was smoothed where required with filler material to restore the model to its original contours. With end-grain balsa wood construction, it is not possible to achieve the high-quality surface finish typically required for performance wind-tunnel testing. However, a good-quality surface finish was achieved. The model was not painted for this test due to concern over protection of the pressure sensor orifices and the surface finish near the orifices. Finally, upper and lower surface transition grit strips were applied. The #80 grit strips were located at 5% chord and were approximately 0.25 in. wide.

Structural Modeling and Vibration Testing

MSC Software's NASTRAN finite element model (FEM) of the clean wing (wing with no tip) configuration from the earlier tests was modified for the current test. In the FEMs, the aluminum plate is represented by bending-membrane-type elements with the plate thickness based on measured values. The four plate thickness steps are shown in Fig. 2a at span stations 18.22, 34.42, 43.52, and

Fig. 3 Wing-tip configurations tested: winglet, pencil tip store, and clean wing tip.

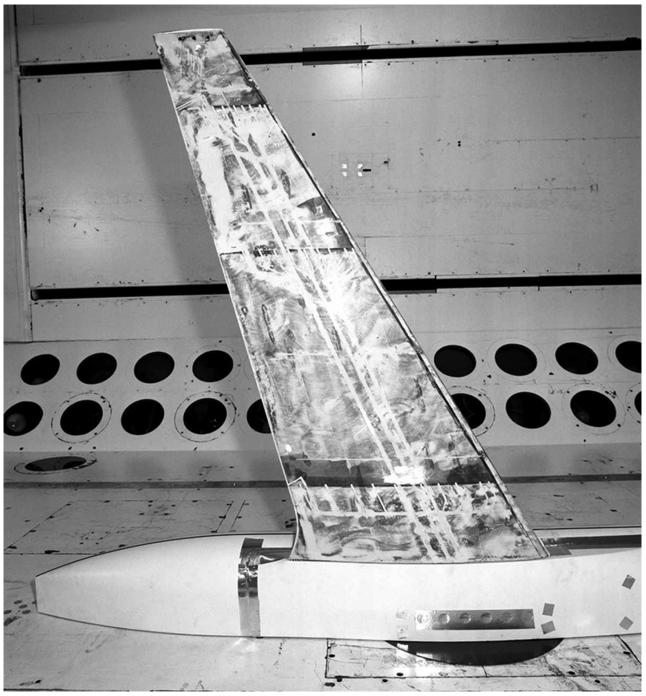

Fig. 4 View of lower wing and fuselage mounted on tunnel sidewall.

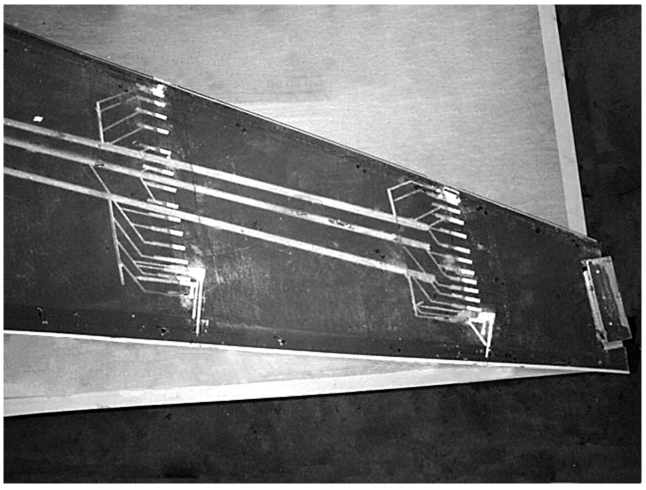

Fig. 5 Upper surface pressure sensor installation showing routing channels during refurbishment of model.

47.84 in. Measured plate thicknesses in the five regions are 0.275, 0.195, 0.155, 0.119, and 0.102 in. The tolerance of the measured thicknesses was ±0.003 in.. On the upper surface of the plate aft of the end-grain balsa wood, the plate was tapered to a thickness of 0.050 in. at the trailing edge. Plate elements representing the end-grain balsa wood, with thickness based on the airfoil shape, are superimposed on the aluminum plate elements. The same balsa properties derived for use in the earlier FEM were used and rendered good quality results in terms of mass and stiffness. New FEMs were constructed for all three of the current tip configurations. Plate and concentrated mass elements were used for the clean wing tip and winglet, and beam elements with concentrated masses were used for the tip store. The final measured and NASTRAN model weights were 24.25, 24.46, and 24.53 lb for the clean wing tip, tip store, and winglet configuration, respectively.

Vibration tests were conducted before the wind-tunnel test and periodically (wind off) during the test. Table 2 gives the pretest analytical and experimental bending and torsion mode frequencies and experimental measured damping values for the three wing-tip configurations tested. The clean wing-tip modal displacements and node lines for the first two bending and torsion modes are shown in Fig. 7. Because of the large wing displacements anticipated for the test, attention was given to ensure that clearances at the wing root were adequate to prevent any rubbing or binding. Large amplitude free decay records indicated smooth damping in the first bending mode, decreasing from 1.5% for ±2.5 in. deflections to 1% at the lowest amplitudes.

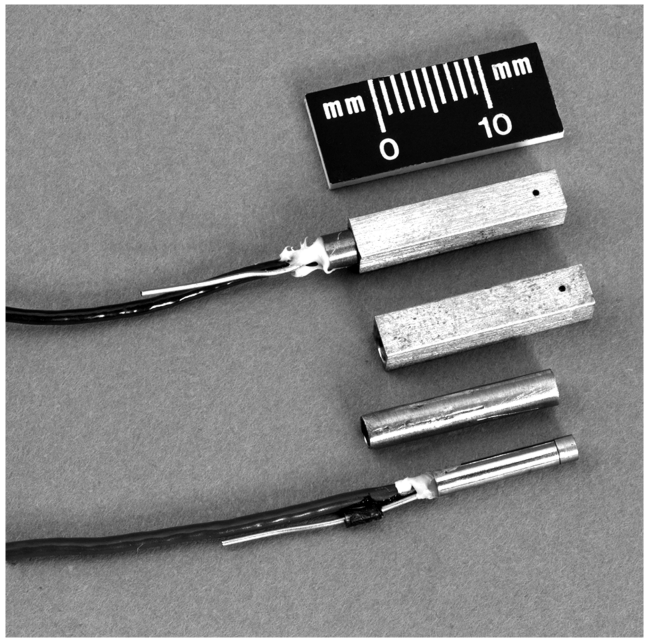

Fig. 6 Unsteady pressure sensor installation components from bottom to top: pressure sensor, protective metal sleeve, rectangular mounting block with orifice hole, and assembled fixture.

The aggressive LCO testing led to some cracks developing in the balsa wood, predominantly in the inboard region of the wing. This was reflected in small changes noted in modal frequencies from the wind-off vibration tests made during the test. For the clean wing-tip configuration, the three lowest frequency modes varied from 4.07 to 3.91, from 14.04 to 12.75, and from 31.76 to 30.32, respectively, over the duration of the test.

Transonic Dynamics Tunnel

The TDT is a closed-circuit, continuous-flow wind tunnel capable of testing at stagnation pressures from near zero to atmospheric conditions and over a Mach number range of 0–1.2. The test section of the TDT is 16 ft^2 with cropped corners. Controlled variation of pressure in the tunnel simulates variations in flight altitude. Tests can

Table 1 Unsteady pressure orifice locations for inboard, middle, and outboard pressure chords

Upper x/C	Lower x/C
0.03	——
0.07	0.07
0.11	0.11
0.16	——
0.22	0.22
0.30	0.30
0.38	0.38
0.44	——
0.50	0.50
0.55	——
0.60	0.60
0.65	——
0.70	0.70
0.76	——
0.82	0.82
0.88	——
0.94	0.94
1.0	——

Table 2 Analytical and experimental structural normal mode frequencies for the three configurations tested

Clean wing tip

	Analysis	Experiment	
Mode	F, Hz	F, Hz	Damping, %
1B	4.08	4.072	1.131
2B	13.97	14.043	1.154
1T	31.54	31.757	0.835
3B	31.99	32.591	1.154
2T	58.11	57.791	0.863
4B	58.79	61.887	1.032
3T	88.23	90.871	0.864
5B	92.21	97.57	1.51

Pencil tip store

	Analysis	Experiment	
Mode	F, Hz	F, Hz	Damping, %
1B	3.68	3.942	1.533
2B	12.89	13.336	1.08
3B	28.91	30.407	1.118
1T	30.53	31.29	0.764
2T	48.73	53.02	1.009
4B	53.97	58.55	1.1224
	71.06	77.61	1.7

Winglet

	Analysis	Experiment	
Mode	F, Hz	F, Hz	Damping, %
1B	3.78	3.815	1.32
2B	11.99	12.294	1.21
3B	25.14	26.279	1.128
1T	30.27	31.027	1.114
Winglet	43.33	45.99	1.039
2T	48.19	50.29	0.948
	62.82	69.66	0.771
	73.14	74.71	0.816

be performed in the TDT using air as the test medium; however, the most distinguishing feature of the tunnel is its ability to accommodate the use of a heavy gas, presently R-134a refrigerant. R-134a is about 4 times as dense as air, yet has a speed of sound of about half that of air. These properties of higher density and lower sonic speed have beneficial effects on the design, fabrication, and testing of aeroelastically scaled wind-tunnel models. Other advantages resulting from the use of a heavy gas are a nearly threefold increase in Reynolds number and lower tunnel drive horsepower requirements.

Data Acquisition System

Two digital data acquisition systems (DAS) were used during the test. The primary system, DAS E, sampled 107 signals, all those discussed earlier plus several tunnel parameters and reference sine waves, at 1000 samples per second (sps). Analog antialiasing prefilters set at 200 Hz were used on all channels. The second system, DAS D, sampled a subset of 30 instrumentation signals at 5000 sps using 1000 Hz prefilters. The DAS D system was intended as a backup for DAS E and to provide information on any high-frequency behavior above the 200 Hz cutoff of the DAS E data. Approximately 1100 tunnel test points were acquired during the test, consisting of test tab points (TP) and flutter bypass points (BP). At tab points, 10 s of data were acquired on both of the DAS systems. Because the TDT is devoted to flutter model testing, it is equipped with a bypass valve system that can rapidly decrease the test section dynamic pressure by venting the back leg of the tunnel circuit to the plenum chamber. The system is activated via a trigger by test personnel in the control room who are monitoring model activity. The data system contains a circular file that continuously maintains data for the preceding 1 min of the test. Activation of the bypass valves initiates acquisition of a BP data point by the DAS. This point consists of the 1 min of data recorded before and 1 min of data acquired after the BP event.

Results

In the present paper, only an overview of the test results will be given. The calculated and experimental flutter boundaries are given for the model in air and heavy gas, followed by a discussion of the flutter and LCO behaviors observed. Finally, maps of the LCO behavior of the model at dynamic pressures of 50–100 psf are given, along with samples of time histories and wing pressure coefficients.

During testing, typical TDT flutter testing procedures were followed. The wing root bending strain gauge was monitored to ensure that limiting bending moments of 2600 in. · lb were not exceeded. Early testing established the root angle of attack for near-zero wing loading as $\alpha = 0.6$ deg. Subsequent testing was performed for the three wing-tip configurations at this angle and at increments of $+1.0$ and $+1.5$ deg, that is, for $\alpha = +0.6, +1.6$, and $+2.1$ deg. Testing was performed at constant tunnel total pressures, typically beginning at the lowest pressure to be tested for a given run and proceeding to higher pressures by "bleeding in" air or heavy gas. At each pressure, tunnel test conditions were established by varying the fan speed (rpm), which simultaneously varied the tunnel Mach number and test section dynamic pressure.

Initial testing at lower dynamic pressures was conducted up to $M = 1.2$. Generally, model response was benign above $M \sim 0.96$ and subsequent testing focused on Mach numbers up to 1.0. Figures 8a and 8b give the flutter boundaries in air and heavy gas for the three wing-tip configurations calculated using the FEMs and

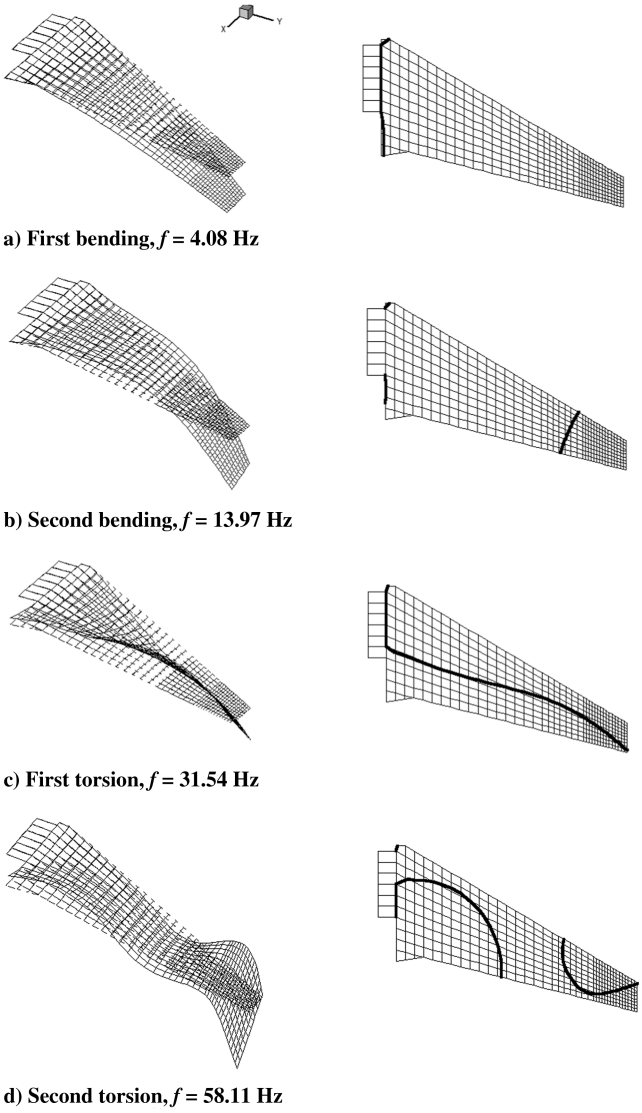

a) First bending, f = 4.08 Hz

b) Second bending, f = 13.97 Hz

c) First torsion, f = 31.54 Hz

d) Second torsion, f = 58.11 Hz

Fig. 7 Mode shapes and node lines for the first two bending and torsion modes of the clean wing-tip configuration.

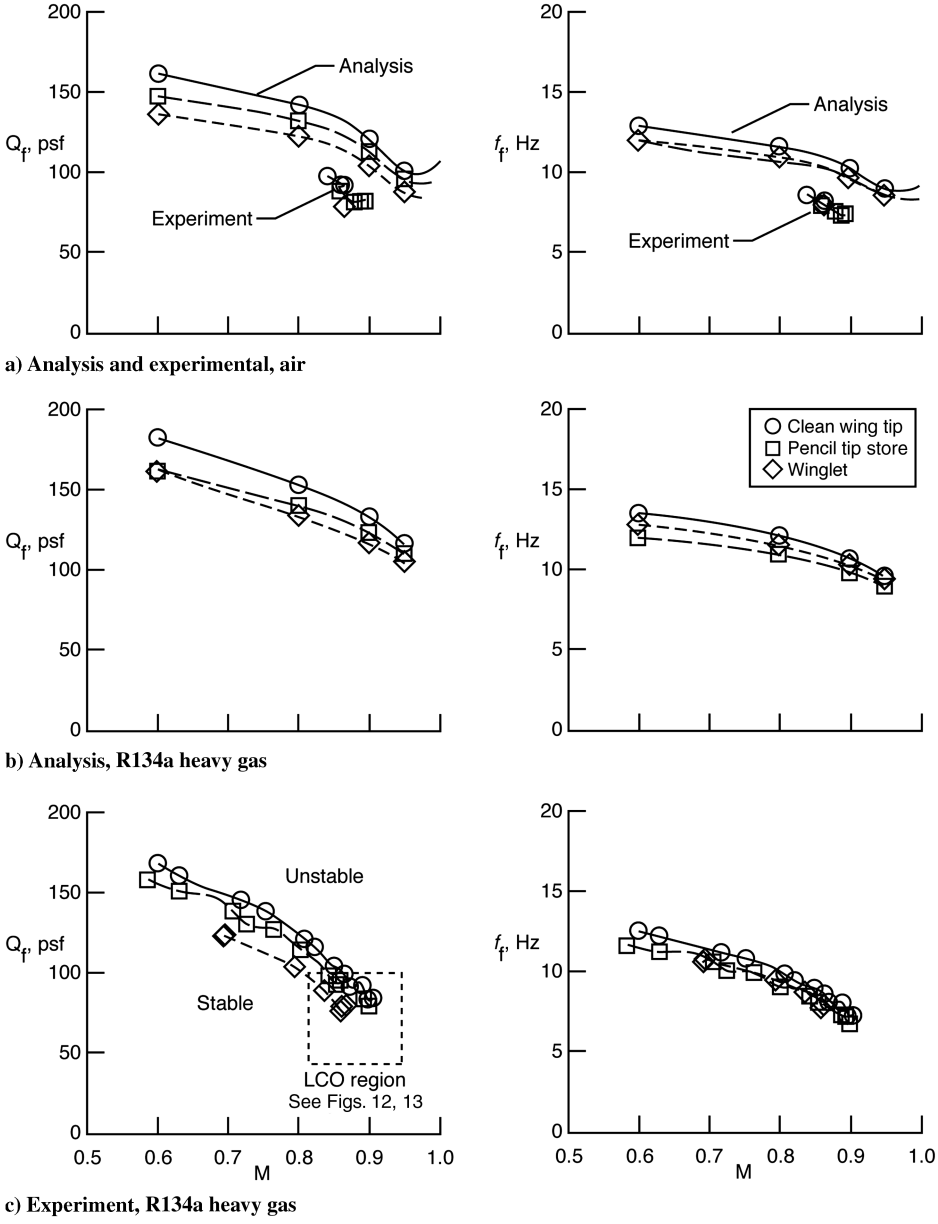

Fig. 8 Flutter boundaries and frequencies in air and heavy gas, $\alpha = 0.6$ deg.

linear doublet lattice aerodynamics. Figure 8a also includes the limited number of experimental flutter points that were obtained in air. Figure 8c presents the corresponding experimental boundaries for heavy gas. The calculated results show similar trends with the Mach number for the model in air and heavy gas, with the flutter boundary in air being about 20 psf lower than in heavy gas. The calculated flutter frequencies are similar for air and heavy gas, dropping from 12–14 Hz at $M = 0.6$ to about 10 Hz at $M = 0.95$. The experimental results in heavy gas (Fig. 8c) show similar trends with each wing-tip configuration, but deviate from the linear calculations for the higher Mach numbers at which the slopes of the experimental results are steeper. At $M = 0.6$, there is good agreement with the linear analysis for the flutter dynamic pressure, Q_f, and frequency, f_f. However, at $M \sim 0.90$, the experimental values of Q_f and f_f have dropped to about 85 psf and below 8 Hz, respectively, well below the corresponding values from the analysis. Figure 9 shows the aft wing-tip accelerometer time history recorded during a typical BP flutter point at $M_f = 0.856$, $Q_f = 92$ psf, and $\alpha = 0.6$ deg for the tip store configuration. The peak amplitude of ± 20 g, when the bypass valves were fired, corresponds to wing-tip displacements of ± 2.9 in. for this $f_f = 8.2$ Hz flutter motion. The flutter analysis indicates that the flutter mode results predominantly from the coalescence of the wind-off first bending and torsion modes at $f = 3.68$ and 29.91 Hz, respectively, for this configuration. The highest f_f measured during the test was at the highest dynamic pressure flutter point in heavy gas ($M_f = 0.595$ and $Q_f = 165$ psf) where $f_f = 12.5$ Hz.

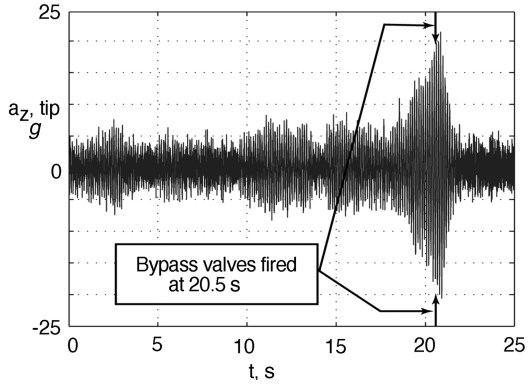

Fig. 9 Sample of an aft wing-tip accelerometer response at a flutter condition, pencil tip store in heavy gas: $M_f = 0.856$, $Q_f = 92$ psf., $\alpha = 0.60$ deg.

The behavior of the model when approaching flutter and LCO points throughout the Mach range of 0.60–0.95 was of interest because it involved elements familiar to flutter test engineers and central to this test: pseudorandom wing response to tunnel turbulence, bursting and beating wing motions, rapid onset of diverging wing oscillations, and the monotonic growth of wing oscillations to constant amplitude, which is the signature of limit cycle oscillations. Response to tunnel turbulence is termed pseudorandom here because there is a correlation with tunnel disturbances, particularly at frequencies below 100 Hz. Bursting wing motions are commonly observed during approaches to flutter conditions and are typified by the sudden growth of wing oscillations, typically of the subcritical flutter mode, whose amplitudes crest and then subside. The duration of these bursts, which occur with irregular intervals, is viewed as an indicator of approaching flutter onset. Beating wing motions are mentioned because they were observed during this test. This behavior is more regular than bursting and is usually associated with closely spaced frequency components. Distinguishing between these latter two behaviors in practice can be difficult. In general, for Mach numbers between 0.60 and 0.85, the Mach number interval between the start of bursting behavior and flutter onset or LCO behavior grows with increasing Mach number. For lower speeds in this range, this difference is small and what is generally termed "classical flutter onset" is observed. That is, over a short interval of increasing Mach number or dynamic pressure, exponentially diverging wing motions are encountered that usually lead to wing failure unless corrective action is taken. At the higher speeds in this range, this difference in Mach number becomes larger and the situation becomes increasingly fuzzy. It is in this region of $M = 0.85$–0.95 that LCO behavior, which does not fit the classical flutter onset model, is encountered for the MAVRIC model.

Figures 10 and 11 present experimental data from a series of test points for conditions near the bottom of the transonic flutter dip. The data are for the clean wing-tip configuration at $\alpha = 0.6$ deg in heavy gas. Figure 10 presents aft wing-tip accelerometer time histories illustrating the model behavior elements discussed earlier, whereas Fig. 11 presents pressure coefficient, C_p, distributions for the outboard row of sensors at the corresponding conditions. The

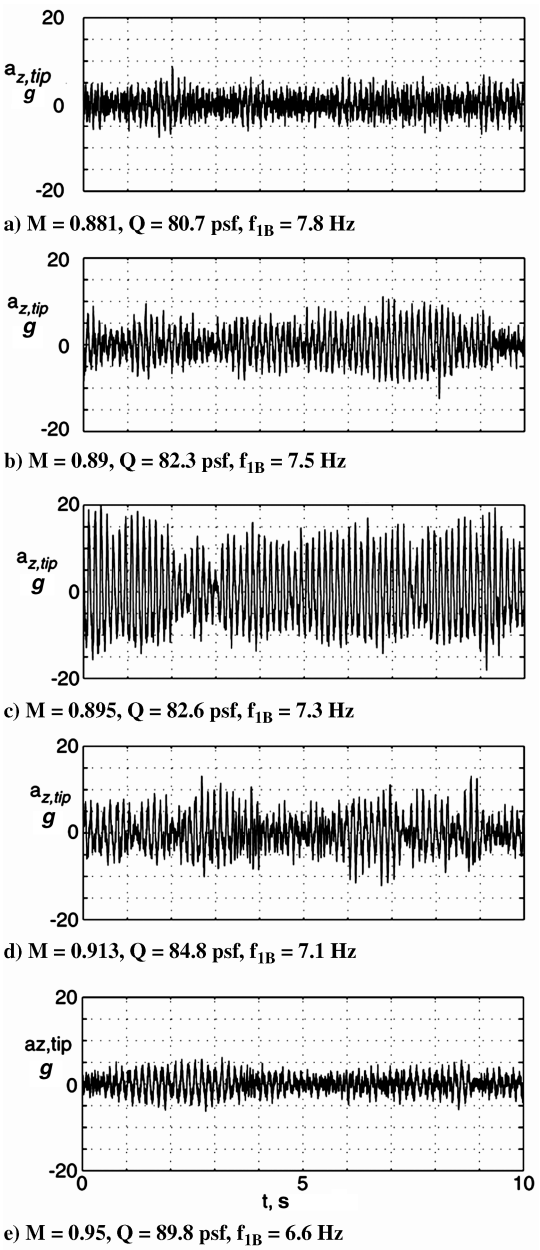

Fig. 10 Sequence of aft wing-tip accelerometer responses exhibiting pseudorandom, bursting, limit cycle oscillation, and beating responses: clean wing tip, heavy gas, $\alpha = 0.6$ deg.

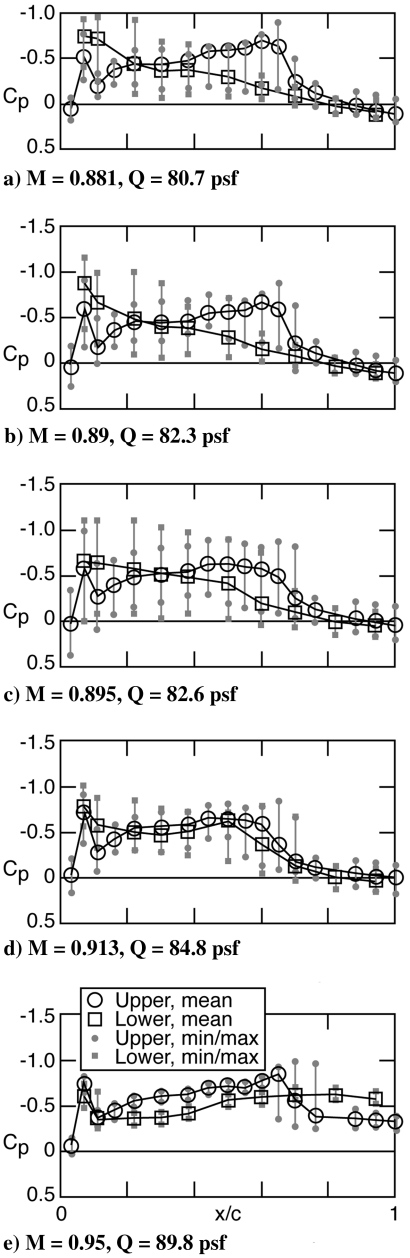

Fig. 11 Sequence of pressure coefficient distributions from the outboard pressure chord at tab points shown in Fig. 10: mean, minimum, and maximum coefficient values.

ranges covered are $M = 0.881$–0.95 and $Q = 80.7$–89.8 psf. The $M = 0.881$ condition (Figs. 10a and 11a) is just below the onset of bursting activity and is characterized by low-level pseudorandom activity in all structural modes up to 200 Hz, with the preponderance of activity in the first and second bending modes (the first bending wind-on frequency, f_{1B}, is 7.8 Hz). Flow at the outboard chord of pressures is intermittently separated at all but the highest Mach number. This is shown in Fig. 11e by the trailing-edge $-C_p$ minimum level rising above 0.0 psi, whereas the maximum level remains below 0.0 psi. At $M = 0.89$, bursting activity in the first bending mode is seen (Fig. 10b) with durations reaching 1–3 s and $f_{1B} = 7.5$ Hz. At this condition, the pressure level minima at the midchord trailing edge, CPU_{100} (not shown), has decreased to 0.0, indicating that the region of separated flow has spread toward midchord. Fully developed LCO occurs at $M = 0.895$, with an average LCO amplitude of about 12 g and with $f_{1B} = 7.3$ Hz. A decreasing frequency of f_{1B} with increasing Mach number has been noted in previous studies documenting high wing response transonic behaviors [12,13], and it is demonstrated here as well. As the separated flow region continues to grow with the Mach number increasing from 0.913 to 0.95, f_{1B} drops from 7.1 to 6.6 Hz. Beating behavior is seen at $M = 0.913$ whereas the response at $M = 0.95$ is much calmer, very similar to that at $M = 0.881$. Note that, at the LCO condition, $M = 0.895$, the trailing-edge wing-tip flow on both the upper and lower surfaces is intermittently separating and reattaching, whereas at $M = 0.95$, with the upper and the lower aft surfaces fully separated at the wing tip (Fig. 11e), the response is benign. Three features that distinguish LCO wind-tunnel testing from flight testing are the test environment, the sensitivity of the LCO behavior, and the wing loading condition. A good portion of the nonstationary nature of the response shown in Fig. 10 is related to the wind-tunnel test environment. First, transonic wind tunnels (even those with documented good flow control and quality) are inherently "noisy" in the frequency range of 0–100 Hz, in which all aeroelastic testing is focused. This is in contrast to the flight-test environment, in which disturbance levels in the 0–100 Hz range are well below those of wind tunnels. Second, a feature seen repeatedly in this test was the sensitivity of the bursting, beating, and LCO behaviors to changing tunnel conditions. A consistent observation was that, when transitioning from one stabilized tunnel condition to another, these dynamic behaviors were invariably accentuated, usually subsiding to lower levels once conditions were stabilized. This was true even for quite slow adjustments to the tunnel condition (accomplished with a low rate of fan rpm changes). Thus, this LCO behavior appears to be due to a very fine balance of forces on the wing, occurring at conditions of intermittent flow separations over wing regions of dominant modal motions (e.g., the wing-tip region here for the first bending and torsion modes).

Finally, the wing loading condition in flight is an important parameter that is very rarely matched in aeroelastic wind-tunnel testing due to the varying similitude requirements for matching model strength versus stiffness. Thus, flutter models are usually tested near unloaded wing conditions ($\alpha \sim 0$) and not near a 1 g statically deformed wing shape that similitude with the 1 g flight test would require. In the LCO maps discussed next, the effect of angle of attack on LCO behaviors is seen to be considerable.

Visual inspection of strip chart time histories for the two wing-tip accelerometers was used to identify regions of bursting, beating, and LCO behavior. Maps of these behaviors are presented in Figs. 12 and 13 for the three wing-tip configurations tested in heavy gas and air, respectively. The maps cover the three angles tested and the dynamic pressure range from 50 to 100 psf. The Mach number range shown is

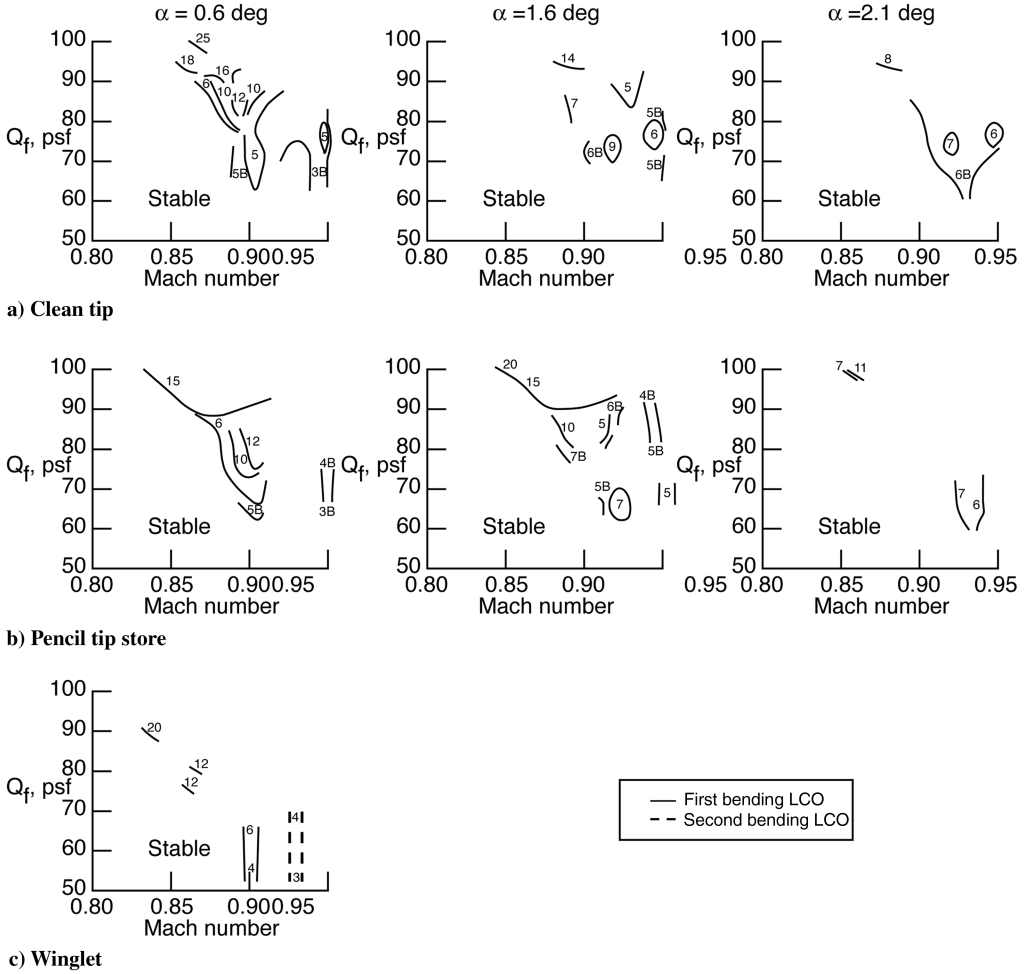

Fig. 12 Maps of limit cycle oscillation regions for model in heavy gas. Indices give half-amplitude levels of aft wing-tip accelerometer response in g; "B" indicates bursting/beating response.

0.82–0.96. Although the model was tested, at the lower pressure levels, to $M = 1.2$, no LCO behavior was observed above $M = 1.0$. Severe Reynolds number and/or transition effects, evident in comparing mean wing pressures for air and heavy gas (not shown), were seen at $Q = 50$ psf. This effect was also noticeable at 75 psf but was not seen at 100 psf. Thus, the LCO map for air, Fig. 13, should be used with caution, whereas that for heavy gas, Fig. 12, is believed to be reliable for transonic flow with turbulent boundary-layer flow. On the other hand, a comparison of the two figures provides insight into the effect of the test gas on LCO behavior, with a particular focus upon the effect of the speed of sound and thus the reduced frequency on LCO for a given model.

The numbers attached to the boundaries in Figs. 12 and 13 give the half-amplitude LCO g-levels for the region denoted by the boundary. Regions of bursting and beating activity are denoted with a "B." The dominant LCO behavior of the model was in the first bending mode, whereas LCO involving the first torsion mode was found for a narrow Mach number range during testing in air. Some regions of small amplitude LCO response of the second bending mode were also observed. Boundaries at the 100 psf level in these figures obviously merge with the flutter boundaries presented in Fig. 8 and define what has traditionally been referred to as the bottom of the transonic dip. This emphasizes the difficulty of distinguishing between flutter and large-amplitude LCO behavior in such regions. Many of these flutter points in Fig. 8 actually were LCO points, even though the amplitude of the wing response led to bypass valve action. Likewise, there were a number of test conditions in the LCO map regions of Figs. 12 and 13 in which the bypass valve was used. The absence of boundaries in certain map regions should not be taken as implying benign response. Because of the complexity of the LCO behaviors, limitations in the number of test points achievable, and concern for model integrity, the coverage of conditions in the maps is neither complete nor continuous.

A consistent feature of the maps, which has been observed elsewhere [2,12–14], is LCO behavior occurring at a constant Mach number over a range of dynamic pressures. Narrowness of these regions leads to use of the term "chimneys" in describing them. A feature notable in the maps is the trend of the dominant first wing bending LCO chimney with the angle of attack. In heavy gas, Figs. 12a and 12b show the Mach number associated with this chimney increasing from $M_{\mathrm{LCO}} = \sim 0.90$ at $\alpha = 0.6$ deg. to $M_{\mathrm{LCO}} = \sim 0.92$ at $\alpha = 2.1$ deg. In contrast to this trend, in air (Fig. 13a and 13b), this LCO chimney decreases in Mach number from $M_{\mathrm{LCO}} = \sim 0.89$ at $\alpha = 0.6$ deg to $M_{\mathrm{LCO}} = \sim 0.87$ at $\alpha = 2.1$ deg. A striking difference in the LCO behaviors of the model in air versus heavy gas is the occurrence of the first torsion mode LCO response in air but not in heavy gas. This occurs consistently in air at $M \sim 0.91$ for all three configurations and all angles of attack. It is possible that this is due to the differing reduced frequencies caused by speed of sound differences in the two gases. The speed of sound in R134a heavy gas is about one-half that in air. Frequency spectra (not shown) of pressures in the vicinity of the shock on the upper surface show energy concentrations at 15–30 Hz in air and 5–15 Hz in heavy gas for data points near $M = 0.91$. These features vary strongly with Mach number. For data points near $M = 0.88$, they are seen at 20–40 Hz in air and 15–25 Hz in heavy gas. For $M = 0.91$, these frequencies result in reduced frequency values of about $k = \omega b/U \sim 0.07$ with b chosen as the semichord at

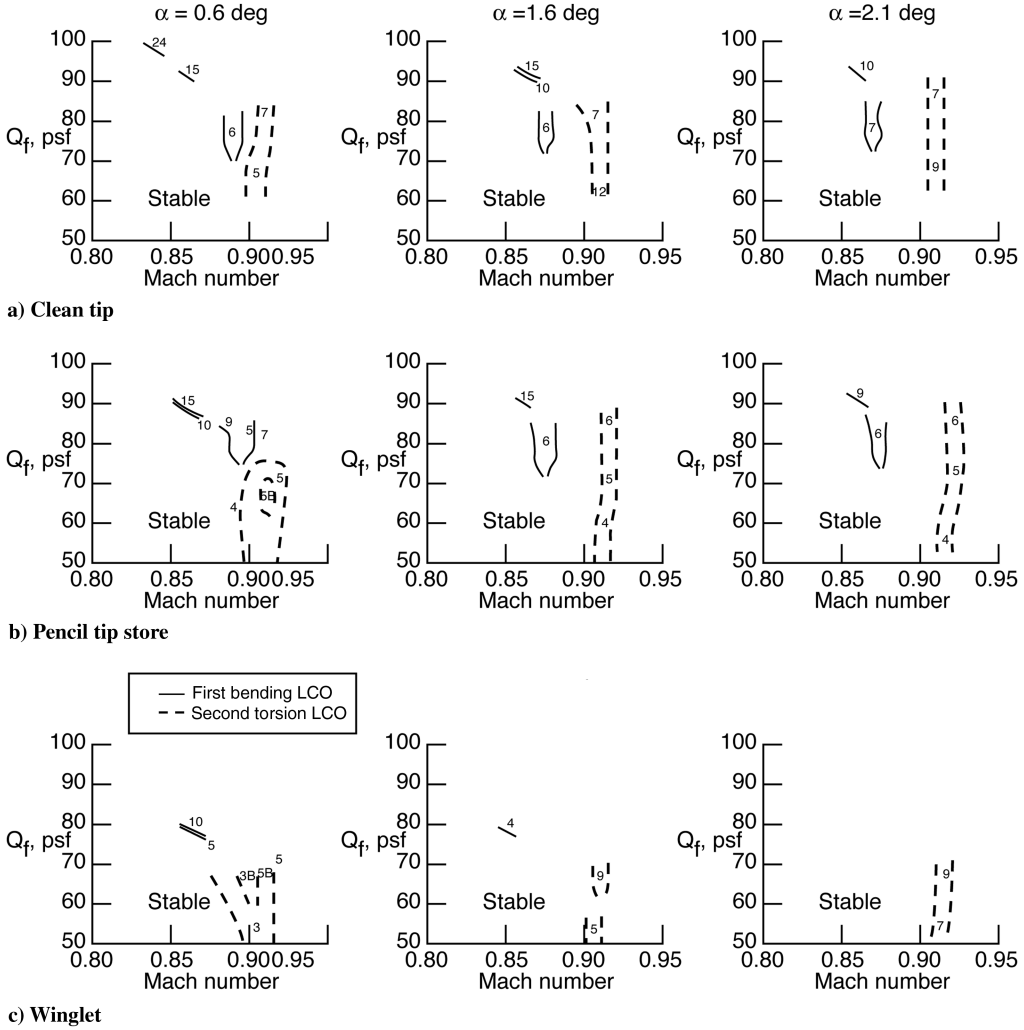

Fig. 13 Maps of limit cycle oscillation regions for model in air. Indices give half-amplitude levels of aft wing-tip accelerometer response in g; "B" indicates bursting/beating response.

the midchord row of pressure sensors. This value is at the low end of the range of reduced frequencies of self-excited shock oscillations that have been measured on airfoils [10]. Thus, a possible coupling mechanism for the first torsion LCO seen here in air is the interaction between shock oscillations and the torsion mode near 30 Hz, whereas, for the same Mach number in heavy gas, the shock oscillation feature is closer to the first bending mode wind-on frequency near 10 Hz.

Discussion of Computational Aeroelasticity Code Simulation of Limit Cycle Oscillation

Computational fluid dynamics codes have held the promise of computing transonic aeroelastic features for many years. The status of applications in this area are documented in [21]. At issue has been achieving the proper level of flow modeling with an economical code capable of performing the numerous computer runs necessary to demonstrate method maturity. The highest code levels encompassing the various implementations of the Navier–Stokes equations have been expensive in terms of computer cost and runtimes, allowing only a small number of sample applications even for attached flow transonic cases. These issues are intensified when considering requirements for resolving the shock–boundary-layer interactions necessary to compute large-amplitude LCO cases such as those presented herein. The capability to treat unsteady shock–boundary-layer interactions for separating and reattaching flows would appear to be a necessity. Inviscid methods are not reliable for such LCO applications [10].

Edwards [10] reported LCO calculations for the 1993 test of the unmodified transport wing flutter model using an interactive quasi-steady boundary-layer method coupled with a transonic small disturbance code. Large-amplitude LCO simulations are shown for $M = 0.888$, $Q = 79$ psf, and $\alpha = 0.2$ deg. The calculations agreed well with the observed model frequency and amplitudes (about 3 in. half-amplitude wing-tip motion) for this test condition in air. The calculation also agreed well with the LCO map from the current test; this condition is contained within the first wing bending LCO region of Fig. 13a ($\alpha = 0.6$ deg).

Conclusions

The MAVRIC, a transport wing flutter model, was tested in NASA Langley's Transonic Dynamics Tunnel with the goal of obtaining experimental data at transonic separation onset conditions typical of limit cycle oscillation behavior. This report gives an overview of the test and wind-tunnel test results. The inexpensive aluminum plate/balsa wood construction and instrumentation procedures used are notable in this research model. Unsteady pressures and wing responses were obtained for three wing-tip configurations: clean, tip store, and winglet. Traditional flutter boundaries were measured over the range of $M = 0.6$–0.9, and maps of limit cycle oscillation behavior were made in the range of $M = 0.85$–0.95. The effects of dynamic pressure and angle of attack were measured. Testing in both R134a heavy gas and air provided unique data on the Reynolds number, transition effects, and the effect of the speed of sound on LCO behavior. Maps of LCO behavior provide insight for this important class of flow conditions involving shock-induced transonic flow separation onset at low wing angles.

Acknowledgments

This work was supported by the NASA Aerospace Systems Concepts to Test program. The authors wish to acknowledge the SEEK EAGLE Office, Eglin Air Force Base, Florida, for support of the structural dynamic modeling and testing and the wind-tunnel testing.

References

[1] Bunton, R. W., and Denegri, C. M., Jr., "Limit Cycle Oscillation Characteristics of Fighter Aircraft," *Journal of Aircraft*, Vol. 37, No. 5, Sept.–Oct. 2000, pp. 916–918. doi:10.2514/2.2690

[2] Denegri, C. M., Jr., "Limit Cycle Oscillation Flight Test Results of a Fighter with External Stores," *Journal of Aircraft*, Vol. 37, No. 5, Sept.–Oct. 2000, pp. 761–769. doi:10.2514/2.2696

[3] Cunningham, A. M., Jr., "The Role of Non-Linear Aerodynamics in Fluid-Structure Interaction," AIAA Paper No. 98-2423, June 1998.

[4] Cunningham, A. M., Jr., "A Generic Nonlinear Aeroelastic Method With Semi-Empirical Nonlinear Unsteady Aerodynamics," Vol. I, U.S. Air Force Research Laboratory VA-WP-TR-1999-3014, Feb. 1999.

[5] Meijer, J. J., and Cunningham, A. M., Jr., "Outline and Applications of a Semi-Empirical Method for Predicting Transonic Limit Cycle Oscillation Characteristics of Fighter Aircraft," *Proceedings of International Forum on Aeroelasticity and Structural Dynamics*, Vol. 2, Royal Aeronautical Society, Manchester, England, U. K., 1995, pp. 75.1–75.19.

[6] Meijer, J. J., "Determination of Transonic Unsteady Aerodynamic Loads to Predict the Aeroelastic Stability of Fighter Aircraft," *Proceedings of CEAS International Forum on Aeroelasticity and Structural Dynamics*, Vol. 2, Associazione Italiana di Aeronautica ed Astronautica, Rome, 1997, pp. 373–383.

[7] Norton, W. J., "Limit Cycle Oscillation and Flight Flutter Testing," *Proceedings of the 21st Annual Symposium*, Society of Flight Test Engineers, Lancaster, CA. 1990, pp. 3-4.4–3.4-12.

[8] Jacobson, S. B., Britt, R. T., Dreim, D. R., and Kelly, P. D., "Residual Pitch Oscillation (RPO) Flight Test And Analysis on the B-2 Bomber," AIAA Paper 98-1805, April 1998.

[9] Dreim, D. R., Jacobson, S. B., and Britt, R. T., "Simulation of Non-Linear Transonic Aeroelastic Behavior on the B-2," *CEAS/AIAA/ICASE/NASA Langley International Forum on Aeroelasticity and Structural Dynamics*, NASA CP-1999-209136, Part 2, NASA Langley Research Center, Hampton, VA, 1999, pp. 511–521.

[10] Edwards, J. W., "Calculated Viscous and Scale Effects on Transonic Aeroelasticity," *Journal of Aircraft*, Vol. 45, No. 6, Nov.–Dec. 2008, pp. 1863–1871. doi:10.2514/1.30082

[11] Gránásy, P., Matsushita, H., and Saitoh, K., "Nonlinear Aeroelastic Phenomena at Transonic Region. CEAS Rome June 1997," *Proceedings of CEAS International Forum on Aeroelasticity and Structural Dynamics*, Vol. 3, Associazione Italiana di Aeronautica ed Astronautica, Rome, 1997, pp. 379–385.

[12] Eckstrom, C. V., Seidel, D. A., and Sandford, M. C., "Unsteady Pressure and Structural Response Measurements on an Elastic Supercritical Wing," *Journal of Aircraft*, Vol. 27, No. 1, Jan. 1990, pp. 75–80. doi:10.2514/3.45898

[13] Eckstrom, C. V., Seidel, D. A., and Sandford, M. C., "Measurements on Unsteady Pressure and Structural Response for an Elastic Supercritical Wing," NASA TP 3443, Nov. 1994.

[14] Silva, W. A., Keller, D. F., Florance, J. R., Cole, S. R., and Scott, R. C., "Experimental Steady and Unsteady Aerodynamic and Flutter Results for HSCT Semispan Models," AIAA Paper 2000-1697, April 2000.

[15] Schuster, D. M., Scott, R. C., Bartels, R. E., Edwards, J. W., and Bennett, R. M., "A Sample of NASA Langley Unsteady Pressure Experiments for Computational Aerodynamics Code Evaluation," AIAA Paper 2000-2602, June 2000.

[16] Knipfer, A., and Schewe, G., "Investigations of an Oscillating Supercritical 2D Wing Section in a Transonic Flow," AIAA Paper 99-0653, Jan. 1999.

[17] Erickson, L. L., "Transonic Single-Mode Flutter and Buffet of a Low Aspect Ratio Wing Having a Subsonic Airfoil Shape," NASA TN D-7346, Jan. 1974.

[18] Farmer, M. G., Hanson, P. W., and Wynne, E. C., "Comparison of Supercritical and Conventional Wing Flutter Characteristics," *Proceedings of the 17th AIAA Structures, Structural Dynamics, and Materials Conference*, AIAA, New York, May 1976, pp. 608–614.

[19] Moss, G. F., and Pierce, D., "The Dynamic Response of Wings in Torsion at High Subsonic Speeds," *44th Meeting of the AGARD Structures and Materials Panel*, CP-226, AGARD 1977, pp. 4-1–4-21; also AGARD Paper 4

[20] Burner, A. W., "Model Deformation Measurements at NASA Langley Research Center," AGARD Paper 34May 1998.

[21] Anon., "Numerical Unsteady Aerodynamic and Aeroelastic Simulation," AGARD R-822, March 1998.